JOURNAL OF SOLID STATE CHEMISTRY **129,** 277–286 (1997)
ARTICLE NO. SC967246

Three Types of Condensed Cluster Phases of Rare-Earth Metal Iodides with Transition Metal Interstitials: Pr_4I_5Ni, Pr_3I_3Os, Pr_2INi_2, and La_2IZ_2

Younbong Park, James D. Martin, and John D. Corbett

Department of Chemistry, Iowa State University, Ames, Iowa 50011

Received August 20, 1996; in revised form November 27, 1996; accepted November 27, 1996

Syntheses of the title compounds result from appropriate reactions of the elements and RI_3 (R = La, Pr) in sealed Nb containers at, variously, 800–990°C. The structures of three were detailed by single crystal X-ray diffraction: Pr_4I_5Ni, *Pmmn*, $Z = 2$, $R(F)/R_w = 3.6/5.3\%$; Pr_3I_3Os, $P2_1/m$, $Z=2$, R/R_w 2.4/2.8%; Pr_2INi_2, $P6_3/mmc$, $Z = 2$, $R/R_w = 2.2/3.6$. The new compounds La_2IZ_2, Z = Fe, Co, Ru, Os, were shown to be isostructural with Pr_2INi_2 (Gd_2IFe_2) by Guinier powder diffraction. Pr_4I_5Ni, the first orthorhombic example among the R_4I_5Z series, consists of R_6Z octahedra condensed into chains. The new example contains the most extreme R:Z size proportions and clearly lacks the strong $d\pi$–$d\pi$ bonding between Z and apical R seen within other members. Pr_3I_3Os, previously known only with a cubic Gd_3Cl_3C-(Ca_3I_3P-)-type structure, also occurs as a relatively undistorted member of the monoclinic Pr_3I_3Ru (double chain) family. Apical Pr–Os π-bonding appears significant, with Pr–Os distances that are 0.24 Å shorter than the average within the waist of the parent octahedra. The R_2IZ_2 phases expand the number of examples of the unusual Gd_2IFe_2 structure, which contains AlB_2-like slabs; namely, graphite-like Z_2 nets between eclipsed pairs of R layers that are in turn separated by single iodine layers. Notable distances in Pr_2INi_2 are Ni–Ni, 2.36 Å, and Pr–Ni, 2.98 Å. Charge-consistent, extended Hückel band calculations in La_2IFe_2 (in contrast with results reported for Gd_2IFe_2) demonstrate a strong mixing of La–Fe and Fe–Fe bonding in a partially filled band, the Fe states on balance falling only slightly below those of La.

INTRODUCTION

Well-reduced rare-earth-metal (R) halide systems exhibit an exceedingly prolific and diverse cadre of novel compounds based on R_6X_{12}-type clusters (1–3). Their most remarkable feature is that these exist, with very few exceptions, only when stoichiometric amounts of a third element Z are present to act as an interstitial stabilizer. Although the last are known to include main-group elements H, B–N, Si, etc., the most versatile and productive Z have come from among the late transition metals from all three periods, viz., Mn–Cu, Ru–Pd, and Re–Au. These are known primarily as iodides rather than chlorides, while the bromides have been investigated less widely (4, 5). The beautiful structural varieties found within these systems start with isolated clusters and different halogen-interbridging modes, all of these being relatively well reduced because of the electron-poor character of the R elements, e.g., as $R_7X_{12}Z$, $R_6X_{10}Z$, and $R_{12}I_{17}Z_2$ (6) stoichiometries. The chemistry also extends to condensed varieties in which clusters share *trans* edges to form chains in monoclinic Pr_4I_5Ru (7), double chains in monoclinic Pr_3I_3Ru (8), and a three-dimensional condensate in the cubic polytype Pr_3I_3Os (9). With further reduction, phases such as (10, 11) R_2X_2C and R_2XZ (12, 14) form in which Z-centered double-metal layers are interleaved by double- and then only single-halogen layers. All told, about 14 structure types are found with heavy metal Z without intruding into the many quaternary cluster phases that contain alkali-metal cations. Complex phase relationships as well as subtleties regarding poorly understood electronic factors and bonding differences are clearly parts of what are often complicated matters of relative phase stability, which outwardly also appear to respond to such obvious factors as the relative sizes of R, X, and Z. With these complexities, it is experimental facts that lead the way. The present article describes just such instances for three types of new compounds: the first orthorhombic chain structure with Pr_4I_5Ni, the monoclinic double-chain phase Pr_3I_3Os where only the cubic 3-D polytype had been seen before, and the double-metal-layered and interstitial-richer Pr_2INi_2 and five La_2IZ_2 phases in a structure for which only the gadolinium–iron analog had been reported (15). The last structure type also provides the opportunity for an improved theoretical description of the bonding in these unusual R–Z_2–R slabs.

EXPERIMENTAL

The general reaction techniques in welded 3/8-in. diameter Nb tubing, the use of Guinier powder photography for both phase identification and approximate yield estimates, and

0022-4596/97 $25.00

the crystallographic characterization means have been described before (4–6). All reactants and products were handled only in gloveboxes ($H_2O < 0.1$ ppm vol). The reagents La and Pr metals (Ames Lab), sublimed RI_3 (prepared from the elements), and powdered Fe (Alfa 99.5%), Ru, Os, Co, Rh, and Ni metals (Johnson-Matthey, $\geq 99.9\%$ metal purity) as interstitials were utilized on 200–300 mg reaction scales.

Syntheses

Pr_4I_5Ni. Its powder pattern was first observed in exploratory reactions loaded with Pr_3I_3Ni to $Pr_{3.3}I_5Ni$ compositions and reacted at 850–890°C for 10 days followed by slow cooling (5°C hr^{-1}) to 700°C. Yields were 70–80% with only PrI_2 and PrOI as the other detectable components. Iodine-richer systems favored production of $Pr_7I_{12}Ni$ (16), and those richer in Pr gave Pr_2INi_2 (below) along with two unknown products.

m-Pr_3I_3Os. Pursuit of a still unidentified phase close to the Pr_3I_3Os composition gave primarily the unknown in high yields in reactions run up to 920°C. But reactions at 990°C also yielded the new m- (monoclinic-) Pr_3I_3Os along with the known phase Pr_4I_5Os (7) when these involved Os-poorer compositions and $Pr_7I_{12}Os$ and $Pr_6I_{10}Os$ (13) with iodine-richer, osmium-poor systems. The previously reported cubic Pr_3I_3Os (9) was not seen following these reactions; its earlier synthesis from stoichiometric reactions had only provided small amounts. The system is quite complicated because of the multiplicity of stable phases. The new cubic Pr_3I_3Au was also encountered during similar explorations.

Pr_2INi_2. Black plates of this phase were obtained at the same time that comparable amounts (40–50%) of one of two other unknown Pr–I–Ni phases were encountered. These particular reactions were loaded as $Pr_{4.5}I_5Ni$ and Pr_3I_2Ni and heated to 860°C for 14 days. $Pr_7I_{12}Ni$ or Pr_4I_5Ni were obtained at higher temperatures (890°C, 25 days) when the same or iodine-richer compositions were used, respectively. Time- and temperature-dependent product distributions have been noted before (4, 8, 9). Several binary Pr–Ni compounds were also identified (17), but these did not appear to be the most stable end products. This structure did not appear to form with Z = Mn, Os, Pd, Pt, or Au.

La_2IZ_2. A series of lanthanum analogs with Z = Fe, Co, Ru, Rh, or Os was also obtained from reactions of LaI_3 with the elements at 800–900°C for 3–4 weeks. These were established to be isostructural with hexagonal Gd_2IFe_2 (15) (Pr_2INi_2) by careful comparison of line positions and intensities in their powder patterns with those calculated with the Pr_2INi_2 coordinates. This product was not obtained with Z = Cr, Mn, Re, Zn while Ni and Cu gave a related but unknown hexagonal structure ($a = 4.138(1)$, 4.250(1), $c = 17.628(4)$, 17.333 (8) Å, respectively).

Single Crystal X-Ray Structures

Pr_4I_5Ni. Weissenberg film studies on a small needle ($\sim 0.03 \times 0.04 \times 0.28$ mm) showed an orthorhombic unit cell $\sim 4.2 \times 9.1 \times 18.9$ Å different from other known phases. Single crystal diffractometer (CAD4) data (Table 1) collected from a hemisphere of reciprocal space ($2\theta < 55°$) for the comparable tuned cell exhibited $0kl$ absences for $k + l = 2n + 1$, which indicated space groups *Pmmn* or $Pmn2_1$ ($R_{ave} = 4.3\%$). Absorption in all three structural studies was corrected for with the aid of the average of several psi-scans. Models produced in the former centric space group by direct methods (18) gave only an incomplete structure through Fourier mapping, but that obtained for the acentric space group allowed all atoms to be located, although some obvious correlations were present. Conversion of the latter set of positions to the centric equivalent quickly yielded an isotropic refinement to $R(F)/R_w = 6.2/8.3\%$, and the anisotropic refinement results were plausible and satisfactory with convergence at $R/R_w = 3.6/5.3\%$.

Pr_3I_3Os. A blade-like crystal ($\sim 0.22 \times 0.09 \times 0.02$ mm) was used. One hemisphere of data collected with the aid of a Rigaku AFC6R diffractometer showed extinctions consistent with space group $P2_1/m$ ($R_{ave} = 2.9\%$). A range of positional parameters and distortions were already known for diverse members of the probable structure type, m-Pr_3I_3Ru (8), so direct methods were used for the structure solution (19). The remainder of the refinement was entirely routine. Application of DIFABS after isotropic refinement of psi-scan-corrected data, as recommended (20), improved the absorption correction for the extreme shape of the crystal employed ($\mu = 372.5\ cm^{-1}$), a procedure that psi-scans do poorly at high θ. The final residuals were $R/R_w = 2.4/2.8\%$.

Pr_2INi_2. Package programs for the Rigaku AFC6R diffractometer and data collected therewith indicated the probable centric space group $P6_3/mmc$, and direct methods provided a model that refined without incident to $R/R_w = 2.2/3.6\%$. The proportions of the plate crystal ($\sim 0.15 \times 0.20 \times 0.02$ mm) and an absorption coefficient of 327.0 cm^{-1} required a DIFABS correction of the isotropic refinement results along the way in order to obtain good results and U_{33} parameters along the thin **c** direction of the crystal that were more comparable to U_{11} and U_{22}.

Powder patterns calculated according to the structural solutions for all three compounds agreed very well with the observed patterns in both line positions and intensities. Some data collection and refinement parameters for all three structures are given in Table 1; the corresponding F_o/F_c data are available from J.D.C.

TABLE 1
Data Collection and Structure Refinement Parameters

Compound	Pr_4I_5Ni	Pr_3I_3Os	Pr_2INi_2
Formula weight	1256.85	993.64	526.12
Space group, Z	*Pmmn* (No. 59), 2	$P2_1/m$ (No. 11), 2	$P6_3/mmc$ (No. 194), 2
Lattice parameters[a]			
a (Å)	4.184(1)	9.146(1)	4.083(2)
b (Å)	18.796(2)	4.303(1)	4.083(2)
c (Å)	9.014(3)	12.334(1)	17.211(6)
α (deg)	90	90	90
β (deg)	90	93.42(1)	90
γ (deg)	90	90	120
Vol. (Å^3)	708.9(5)	484.5(2)	248.5(2)
d_{calc}(g/cm^3)	5.88	6.81	7.03
Crystal size (mm)	$0.28 \times 0.04 \times 0.03$	$0.22 \times 0.09 \times 0.02$	$0.15 \times 0.20 \times 0.02$
Diffractometer (Mo$K\alpha$)	CAD4	AFC6R	AFC6R
Temp. (°C)	22	23	23
$2\theta_{max}$(deg)	55	50	50
Scan method	ω	$2\theta - \omega$	$2\theta - \omega$
Octants measured	$h, \pm k, \pm l$	$h, \pm k, \pm l$	$h, \pm k, l$ $(h \geq k)$
No. of refl. measured	3457	1827	288
observed ($I > 3\sigma_I$)	1012	1395	248
unique observed	622	757	104
μ (Mo$K\alpha$, cm^{-1})	255.1	372.6	327.0
Rel. transm. factors	0.50–1.0	0.85–1.0	0.72–1.0
R_{ave} ($I > 0$), %	4.3	2.9	3.1
No. of variables	36	44	10
Final R/R_w[b] (%)	3.6/5.3	2.4/2.8	2.2/3.6
Max. shift/esd (last cycle)	0.00	0.00	0.00
Largest ΔF peak, e$^-$/Å^3	5.3(0.76 Å from Pr2)	2.2 (1.63 Å from Pr2)	1.8
Sec. extinct. coeff. (10^{-7})	1.8(3)	2.3(2)	3(2)

[a] Guinier powder data with Si as internal standard ($\lambda = 1.54056$ Å).
[b] $R = \sum||F_o| - |F_c||/\sum|F_o|$; $R_w = [\sum w(|F_o| - |F_c|)^2/\sum w(F_o)^2]^{1/2}$; $w = \sigma_F^{-2}$.

Band Calculations (21)

The three-dimensional, tight-binding band calculations for La_2IFe_2 utilized its lattice constants and the fractional coordinates of Gd_2IFe_2 and was carried out at 252 k-points. The standard (default) H_{ii} parameters for La and Fe were iterated to charge consistency to give La: 5*d*, −7.83; 6*s*, −6.82; 6*p*, −4.58 eV; Fe: 3*d*, −8.72; 4*s*, −6.67; 4*p*, −3.37 eV (22, 23), while those for I: 5*s*, −20.8; 5*p*, −11.2 eV came from the charge-consistent calculations done earlier on $Y_6I_{10}Ru$ (24). The Fe values so obtained are slightly less negative than these reported for the element (−9.2, −7.6, −3.8 eV, respectively) (23). The orbital exponents used were, as before, the standard default values.

RESULTS AND DISCUSSION

Orthorhombic Pr_4I_5Ni

Table 2 lists the positional and thermal parameter data, Table 3 gives some important distances, and Fig. 1 shows the structure of Pr_4I_5Ni projected down the short a (chain) axis. This orthorhombic structure is remarkable as the first polytype of the monoclinic R_4I_5Z series known for transition metal Z in La_4I_5Ru and Pr_4I_5Z, Z = Co, Ru, Os (7), but not for any Pr_4Br_5Z (4). (Y_4I_5C (25) and Gd_4I_5Z, Z = C or Si (26), are also isotypic.) $Pr_6(Z)$ octahedra again share pairs of *trans*-edges to form quasi-infinite chains along the short axis, with all exposed edges bridged by iodine (I^i) and exposed vertices of the octahedra bonded exo to edge-bridging iodine (I^{a-i}) in the adjoining chains. The sheets of chains so generated along the long (vertical) axis are inter-bridged along the axis of intermediate (~9 Å) length by bifunctional I^{i-i} bridges at the waists of the octahedra, as shown.

The [100] view in Fig. 1 along the chains in Pr_4I_5Ni shows how the pairs of complementary $I2^{i-a}$ bridges at the top and bottom of each octahedron lie on the same side of the chain, following the fact that the waists of the octahedra along the chains lie on mirror planes. All atoms also lie on mirror planes at $x = 1/4$, 3/4, and the symmetry at Ni is

TABLE 2
Positional Parameters and Anisotropic Displacement Parameters for Pr_4I_5Ni

Atom	Position	y^a	z	$B_{eq}{}^b$
Pr1	2*b*	3/4	0.6603(2)	1.36(7)
Pr2	2*b*	3/4	0.0830(2)	1.32(7)
Pr3	4*e*	0.39649(6)	0.1312(2)	1.37(4)
I1	4*e*	0.57959(7)	0.6063(2)	1.53(6)
I2	4*e*	0.57596(7)	0.1400(2)	1.40(5)
I3	2*a*	1/4	0.6288(3)	2.15(8)
Ni	2*a*	1/4	0.1255(6)	1.3(1)

Atom	$U_{11}{}^c$	U_{22}	U_{33}	U_{23}
Pr1	0.0157(8)	0.0116(8)	0.024(1)	0
Pr2	0.0153(8)	0.0112(8)	0.0237(9)	0
Pr3	0.0189(6)	0.0163(6)	0.0168(5)	0.0002(6)
I1	0.0194(7)	0.0177(7)	0.0210(8)	−0.0051(6)
I2	0.0198(7)	0.0139(6)	0.0197(7)	0.0024(7)
I3	0.0152(9)	0.046(1)	0.021(1)	0
Ni	0.024(2)	0.010(2)	0.017(2)	0

[a] Origin at $\bar{1}$. All atoms have $x = 1/4$.
[b] $B_{eq} = (8\pi^2/3)\sum_i\sum_j U_{ij}a_i^*a_j^*\mathbf{a}_i\mathbf{a}_j$.
[c] $T = \exp[-2\pi^2(U_{11}h^2a^{*2} + U_{22}k^2b^{*2} + U_{33}l^2c^{*2} + 2U_{23}klb^*c^*)]$, $U_{12} = U_{13} = 0$.

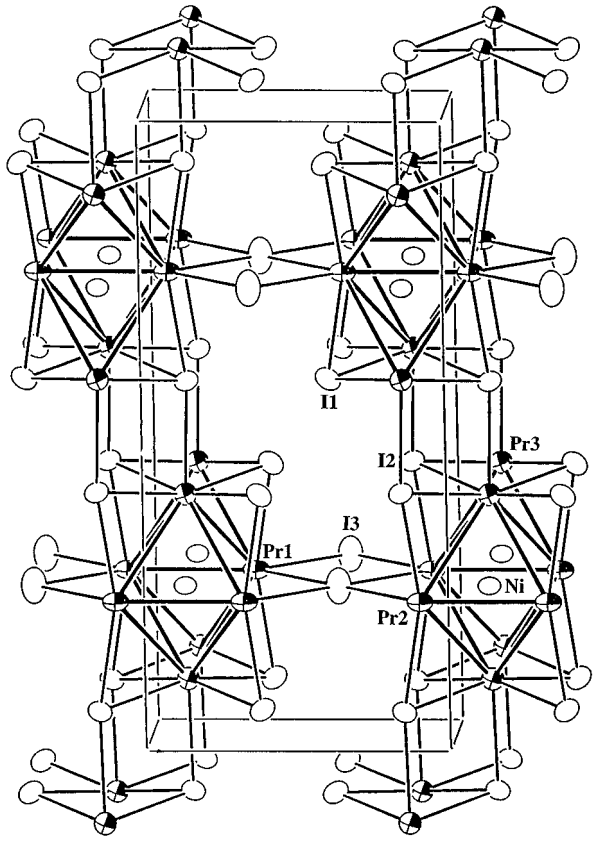

FIG. 1. ~ [100] section of the orthorhombic Pr_4I_5Ni structure with *b* vertical. Pr atoms are shaded, and I and Ni atoms (at the cluster centers) are open (90%) ellipsoids.

*mm*2 (C_{2v}). In the monoclinic R_4I_5Z family, a 2-fold axis runs along the chains instead, so that the I^{i-a} bridging connections lie on opposite sides of each octahedron when viewed along the chains. This in effect gives a twist to all the chains along the projection (*b*) axis to generate a monoclinic cell with a 104.6° angle between what are in the present structure the rectalinear *b* and *c* axes. The symmetry at Ru is thus 2/*m* (C_{2h}).

TABLE 3
Selected Bond Distances in Pr_4I_5Ni[a]

Pr1–Pr2	×2	3.811(3)
Pr1–Pr3	×4	3.936(2)
Pr1–I1	×2	3.240(2)
Pr1–I3[b]	×2	3.342(3)
Pr1–Ni	×2	3.847(4)
Pr2–Pr3	×4	3.961(2)
Pr2–I2	×2	3.312(1)
Pr2–I3[b]	×2	3.335(3)
Pr2–Ni	×2	2.813(4)
Pr3–I1	×2	3.190(2)
Pr3–I2	×2	3.259(2)
Pr3–I2[b]		3.374(2)
Pr3–Ni		2.754(1)
I1–I1	×2	4.123(3)

[a] All atoms also have two like members at 4.184(1) Å, the *a* axis repeat.
[b] Interchain bridge.

Notable differences in size proportions and in bonding in the two chains are probably responsible for the structural change. Detailed considerations of the interstitial bonding in Pr_4I_5Ru were previously pursued (7) in part because of notable differences in cluster and chain proportions between Pr_4I_5Ru and the only other refined analogs available at that time, the isostructural Y_4I_5C and Gd_4I_5Si. Remarkably, much of the same differences now appear between what would be thought to be the much more similarly bonded Pr_4I_5Ru and Pr_4I_5Ni. Some characteristic dimensions of the two are compared and contrasted in Table 4. Those features that do not change much are both the waist–apex Pr–Pr distances and the Pr–Pr distances over the octahedra which average only 0.04 Å greater for Ru. Of course, these relatively long Pr–Pr bond lengths are fixed principally by characteristic radii of Pr and *Z* (a matrix effect) and, likewise, the average Pr–*Z* distances of 2.805 Å (Ni) vs 2.829 Å (Ru) appear to reflect only a plausible increase in interstitial size. (The single bond metallic radii differ by 0.092 Å (27).)

TABLE 4
Comparative Distances (Å) in Pr_4I_5Ni and Pr_4I_5Ru

		Pr_4I_5Ni (A)	Pr_4I_5Ru (B)[a]	Δ(B–A)
1	Axial repeat, Pr–Pr	4.184(1) (*a*-axis)	4.265(1) (*b*-axis)	0.081
2	Shared edge, Pr–Pr	3.811(3)	4.041(2)	0.230
3	Pr–Pr (waist-apex)$_{ave}$	3.948	3.930	− 0.018
	Δ(2–3)	− 0.137	0.111	0.248
4	*Z*–Pr (waist)$_{ave}$	2.830	2.938(1)	0.108
5	Pr–*Z* (apex)	2.754(1)	2.611(1)	− 0.143
	Δ(4–5)	0.076	0.327	0.251
	ave. (4, 5)	2.792	2.775	− 0.017
6	Pr–I^{a-i}	3.374(2)	3.450	0.076

[a] Ref. 7.

Among the more notable differences (Table 4) are the appreciable reapportionment of the rectangular waists of the condensed clusters from Ni to Ru, an increase of 0.08 Å in the Pr–Pr chain repeat distance but even a greater increase in the shared Pr–Pr edge, 0.23 Å. These presumably "follow" the other major difference between the two Pr_4I_4Z members, the individual *Z*–Pr distances. For Ni, those within equitorial plane (waist) are only 0.08 Å larger than that to the apices, in contrast to a 0.33 Å difference with Ru. In other words, the clusters in Pr_4I_5Ru are markedly flattened normal to the chain. The Pr–Pr and, especially, Pr–*Z* differences in Table 4 are semiquantitatively the same as between Gd_4I_5Si and Pr_4I_5Ru, for which detailed charge-consistent calculations and analysis showed that the comparable changes originate with particularly good d_{yz}–d_{yz} Pr–Ru π (and σ) bonding to the apicies in the flattened and elongated octahedra that is of course absent with Si (*x* is the chain axis) (7). (The major Ru contributions to the DOS were observed to fall just below and around E_F.) A parallel phenomenon for Ni vs Ru follows, apparently because of distinctly poorer $d\pi$ bonding with the smaller and lower lying Ni *d* orbitals, plus a two-electron further reduction. The 3*d* orbitals of Ni in another strongly reducing environment, $In_{10}Ni^{10-}$, have also been found to be basically core-like (28), and a similar withdrawal of 3*d* orbitals is evident in a series of La_5Ge_3Z and $La_{15}Ge_9Z$ phases for Z = Fe–Ni (29). The general trend of 3*d* energies in the metals has been theoretically considered in detail (30).

Changes in exo *R*–I bond lengths commonly reflect differences in the opposed *R*–*Z* bonding, among other things (2), and so it is here. The Pr3–I2^{a-i} bonds are 0.08 Å shorter at the more exposed Pr vertex with Ni than for the equivalent bond in the ruthenide, where the opposed *R*–*Z* distance is much less. The other *i*–*a* bonds to I2 in Pr_4I_5Ni are correspondingly a little longer ($\sim$0.03 Å). The reasons for the formation of the new structure, with its changes in chain packing and bridging, remain somewhat obscure, but they probably arise in good part from fairly subtle differences in charge dispositions and in closed-shell I ⋯ I repulsions. The shortest interchain I1 ⋯ I1 contacts in Pr_4I_5Ni (4.123 Å) are 0.044(4) Å less than those found in Pr_4I_5Ru, as are the next shortest repeat distances for all atoms along the chain direction (4.184 Å). The fact that Ni interstitial is the smallest accommodated within an early lanthanide metal cluster halide must be important. It is noteworthy that the cell volume of the neighboring monoclinic Pr_4I_5Co (Pr_4I_5Ru type) is 1.9% greater than that of Pr_4I_5Ni, but only 0.4% less than that of Pr_4I_5Ru. Still smaller interstitial atoms like carbon have been accommodated in this structure type only with smaller *R*, in Y_4I_5C, Gd_4I_5C, and so forth.

Monoclinic Pr_3I_3Os

The positional and thermal parameters for this structure are listed in Table 5, and its important distances appear in Table 6. Figure 2 gives a [010] view down the short axis and along the double chains, which now can be imagined to result from a side-by-side condensation between pairs of the single chains seen in Pr_4I_5Ni, etc., that have relative displacements of *b*/2.

Two matters of importance concern this compound and structure, the distortion and the stability range. A series of monoclinic R_3I_3Z phases have been found to show a remarkable continuous distortion, increasing roughly in the order R = La, *Pr*, Gd, *Y*, or Er with fixed Z = Ru, and then for R = Gd, *Y* with Z = Ir (8). Single crystal refinements for phases with the three *R* listed above in italics gave the best

TABLE 5
Positional and Displacement Parameters[a] for Monoclinic Pr_3I_3Os

Atom	*x*	*y*	*z*	B_{eq}
Pr1	0.09965(9)	1/4	0.89011(7)	1.00(3)
Pr2	0.11899(9)	1/4	0.33572(8)	1.16(4)
Pr3	0.31416(9)	3/4	0.12111(7)	1.09(3)
I1	0.3943(1)	3/4	0.86307(9)	1.30(4)
I2	0.3747(1)	3/4	0.38153(9)	1.51(4)
I3	0.1383(1)	1/4	0.61779(9)	1.41(4)
Os	0.11058(6)	1/4	0.12287(5)	0.90(3)
Atom	U_{11}	U_{22}	U_{33}	U_{13}
Pr1	0.0129(4)	0.0134(5)	0.0115(5)	0.0003(3)
Pr2	0.0183(4)	0.0138(5)	0.0119(5)	0.0009(3)
Pr3	0.0119(4)	0.0161(5)	0.0133(5)	0.0014(3)
I1	0.141(5)	0.0162(6)	0.0193(6)	0.0019(4)
I2	0.0199(5)	0.0191(6)	0.0178(6)	−0.0045(4)
I3	0.0207(5)	0.0185(6)	0.0147(6)	0.0024(4)
Os	0.0127(3)	0.0101(3)	0.0114(3)	0.0012(2)

[a] $U_{12} = U_{23} = 0$.

TABLE 6
Selected Bond Distances (Å) and Angles (°) in Pr_3I_3Os[a]

Pr1–Pr1		3.986(2)	Pr1–I1	×2	3.480(1)
Pr1–Pr2	×2	3.965(1)	Pr1–I3	×2	3.398(1)
Pr1–Pr3		3.779(1)	Pr2–I2	×2	3.203(1)
Pr1–Pr3	×2	3.991(1)	Pr2–I3		3.473(2)
Pr2–Pr3	×2	3.922(1)	Pr2–I3	×2	3.264(1)
			Pr3–I1		3.308(1)
Pr1–Os		2.867(1)	Pr3–I1	×2	3.422(1)
Pr1–Os	×2	2.8836(8)	Pr3–I2		3.227(1)
Pr2–Os		2.622(1)			
Pr3–Os	×2	2.8462(8)	I2–I2		4.198(2)
Os–Os	×2	4.144(1)			
Pr1–I1–Pr1		76.38(3)	Pr1–Os–Pr2		179.69(3)
Pr1–I1–Pr3	×2	71.97(3)	Pr1–Os–Pr2	×2	92.02(3)
Pr1–I1–Pr3		171.23(4)	Pr1–Os–Pr3		82.52(3)
Pr3–I1–Pr3	×2	99.31(3)	Pr1–Os–Pr3	×2	88.63(3)
Pr3–I1–Pr3		77.91(3)	Pr1–Os–Pr3		176.31(4)
			Pr2–Os–Pr3	×2	91.57(3)
Pr1–Os–Pr1	×2	87.77(3)	Pr3–Os–Pr3		98.21(3)
Pr1–Os–Pr1		96.52(2)			

[a] All atoms have like two neighbors at 4.303 Å, the chain repeat distance (*b*).

quantification of how the two condensed chains seen in Fig. 2 distort and effectively merge. This can be visualized as the opposed displacements of the upper five and lower five *R* atoms (and *Z*) in each octahedron along $\pm a$ until two interstitials fall more-or-less above one another. The ordering of the degree of distortion for the others in the above series for which only powder data were available was based on the apparent parallel decrease in the *a*/*b* axial ratio. This means the distortion generally appears to increase for smaller *R* or larger *Z*. (The axial ratio for Pr_3I_3Os alone places it between Pr_3I_3Ru and Gd_3I_3Ru). The distortion seems to be driven by significantly more *R*–*R* as well as additional *Z*–*Z* bonding at the extreme, but the analysis is complicated by the presence of the smaller yttrium in the series above, and the larger and electron-richer interstitial Ir in the last as well.

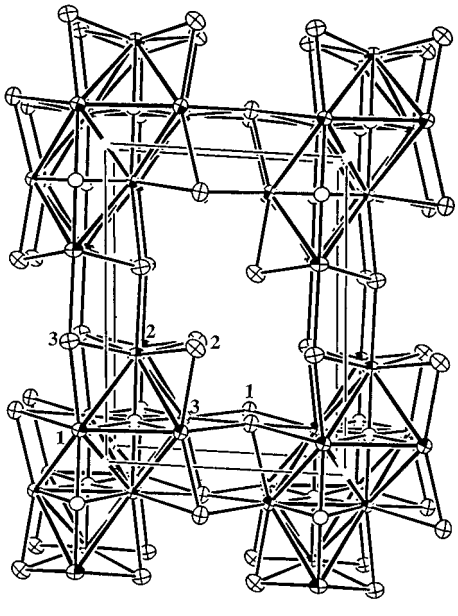

FIG. 2. ~ [010] view of monoclinic Pr_3I_3Os with *c* vertical. Note that pairs of condensed chains, as in Fig. 1, have been condensed side-by-side. The Pr are shaded, I crossed, and Ni open 90% ellipsoids.

The present Pr_3I_3Os results help sort out the factors by allowing a much closer comparison with Pr_3I_3Ru, and the two in fact turn out to be very similar. One useful measure of the degree of distortion appears to be the deviation of the apical *trans* angle Pr1–*Z*–Pr2 in each octahedral chain from 180° (Fig. 2). This increases slightly from 179.4° with Ru to 179.7° with Os, in contrast to ~154° at the distortion extreme Y_3I_3Ir. (The angle drops to 174.7° for the first listed earlier, La_3I_3Ru (14), so size proportions also play a rile.) The average d(Pr–*Z*) for Ru vs Os increases by a plausible amount for the larger interstitial, ~0.007 Å vs a 0.014 Å difference in the single metallic bond radii between Os and Ru (27). (Os is 0.011 Å larger than Ru judging from the corresponding $\bar{d}$(Y–*Z*) values in $Y_6I_{10}Z$ phases, which contain isolated clusters interbridged by iodine (16).) Remarkably, the axial Pr2–*Z* distances are again substantially shortened from the average Pr(1, 3)–*Z* in both Pr_3I_3Z phases, by 0.296 Å (Ru) and 0.243 Å now (Os). These appear to reflect the presence of the same strong $d\pi$–$d\pi$ bonding already noted in the single chains in Pr_4I_5Ru. A clear π bonding behavior appears absent in Y_3I_3Z as other distortions dominate.

The close comparison possible between two Pr_3I_3Z examples with group 8 interstitials Ru and Os now makes it clearer that the extreme distortions seen in R_3I_3Ir arise more because of the smaller *R*, Y, and Gd, although the role of the electron-richer *Z* is not clear. At the other extreme, the isopointal Gd_3I_3Mn, with both smaller metal components and an electron deficiency, exhibits even more distortion and clearly increased Mn–Mn bonding (31). These features have not received theoretical study. We have also noted sizeable decreases in tetragonal distortions in isolated clusters for $Y_6I_{10}Z$ over the series *Z* = Ru, Os, Ir, and these led us to suggest that relativistic effects might also be involved for the Ru–Os change (4, 16). However, Pr_3I_3Ru and Pr_3I_3Os show no significant and otherwise inexplicable differences that might support such a general complication.

Finally, we need to comment on the stability and appearance, or not, of these phases as a function of *Z* and alternative products. We earlier concluded that the formation of cubic R_3I_3Z phases with large *R* seemed to be favored by 5*d* interstitials Os, Ir, and Pt, while the present monoclinic

structure was favored by the 4*d* element Ru over a range of *R* (La–Er) as well as for the electron-richer Ir when *R* is small (Y). The distinction was sharper with Pr_3Br_3Z, where the cubic structure occurred for Co, Rh, and Os–Pt, while a monoclinic phase was found only with Pr_3Br_3Ru (4). Even so, synthesis experiments involving multiple phases are sometimes complex in a kinetic (time) as well as a thermodynamic sense (4, 8, 9) (see Experimental, Synthesis). Still, it is striking that the present Pr_3I_3Os composition was previously identified (albeit in low yield, via its distinctive Guinier pattern) (9) solely in the cubic Gd_3Cl_3C (Ca_3PI_3-type) structure (32) in which each cluster shares three edges with others to generate a complex helical network, yet this polytype was never encountered in the present work. The complexities of these systems presumably leave room for such variations, which again bring to mind how difficult it is to conclude with certainty that a given phase is unstable and can "never" be made.

Pr_2INi_2 and La_2IZ_2

These add to a formerly short list of isomorphous phases with this unusual metal-rich layered structure and transition metal interstitials, namely Gd_2IFe_2 and Gd_2ICo_2 (15, 33). The positional and displacement ellipsoid data and distances for Pr_2INi_2 are listed in Table 7 (other data are in Table 1), while lattice constants for La_2IZ_2, Z = Fe, Ru, Os, Co, Rh, are given in Table 8. Figures 3 and 4 show views of the structure ($P6_3/mmc$) of Pr_2INi_2 normal and parallel to the unique *c* axis, which views are in the opposite sense parallel and normal to the (Pr–Ni–Pr–I) layering sequence, respectively. The triple metal layers contain Ni in all trigonal prismatic cavities between pairs of eclipsed (rather than close-packed) Pr layers. This disposition generates graphite-like Ni layers with short Ni–Ni distances, $a/\sqrt{3} \simeq 2.358$ Å. The AlB_2 structure contains the same layered network unit, but in Pr_2INi_2 these are not condensed but separated by single iodine layers that project onto alternate Ni positions (Fig. 3). This halogen asymmetry is presumably responsible for the very slight ($\pm$ 0.03 Å) puckering of the Ni layer. The structure appears to be clearly dominated by strong metal–metal bonding in the R_2Z backbone.

TABLE 8
Lattice Constants of La_2IZ_2 Phases[a]

	a	*c*	*a*/*c*	*V*
La_2IFe_2	4.116(2)	18.121(8)	0.2271	265.87
La_2ICo_2	4.0883(9)	17.899(4)	0.2284	259.09
La_2IRu_2	4.2996(7)	17.820(7)	0.2413	285.30
La_2IRh_2	4.119(1)	17.65(2)	0.2334	259.3
La_2IOs_2	4.2995(4)	17.972(5)	0.2392	287.72

[a] $P6_3/mmc$, Gd_2IFe_2 type. From Guinier powder diffraction data with Si as internal standard, λ = 1.54056 Å, 22°C.

In addition to the isotypic La_2IZ_2 phases listed in Table 8, we were also able to synthesize apparent La_2IZ_2 phases for Ni and Cu, but close comparisons of their powder pattern details showed that these do not have exactly the same structure as do $La_2I(Fe, Co)_2$, Pr_2INi_2, and $Gd_2I(Fe, Co)_2$ ($P6_3/mmc$). Substantial changes in some line intensities are evident, especially for *h*0*l* reflections with *l* odd, but the details of the structural changes have not yet been worked out. The simple hexagonal lattice (or sublattice) constants for the whole series Fe–Cu show a 0.8 Å (4.5%) contraction in *c*, while *a* expands by 0.13 Å. This parallels a distinct flattening of the *R*–*Z*–*R* slabs seen in single crystal data for the series Gd_2IFe_2, Gd_2ICo_2, and Pr_2INi_2, where the ratio of the *R*–*R* distances across the slab (Fig. 3) to the **a** repeats decreases regularly (0.928, 0.914, 0.898 : 1). We presume this has an electronic origin in the increasing electron count for and the decreasing size of *Z*.

The foremost structure type among the halides with double-metal-layered rare-earth elements is probably the

TABLE 7
Atomic Positional and Displacement Parameters for and Important Distances (Å) in Pr_2INi_2

Atom	*x*	*y*	*z*	B_{iso}	U_{11}[a]	U_{33}
Pr	0	0	0.10617(7)	1.06(4)	0.0138(6)	0.0127(9)
I	2/3	1/3	1/4	1.18(6)	0.0128(7)	0.015(1)
Ni	1/3	2/3	0.0017(2)	1.17(7)	0.013(1)	0.019(1)

		distance			distance		distance
Pr–Pr		3.665(3)	Pr–Ni	×3	2.965 (2)	Pr–Pr	
Ni–Ni	×3	2.358(1)	Pr–Ni	×3	3.001(2)	Ni–Ni	4.083(2)[b]
Pr–I	×3	3.418(1)				I–I	

[a] $U_{22} = 2U_{12} = U_{11}$; $U_{13} = U_{23} = 0$.
[b] The *a*, *b* axial repeats.

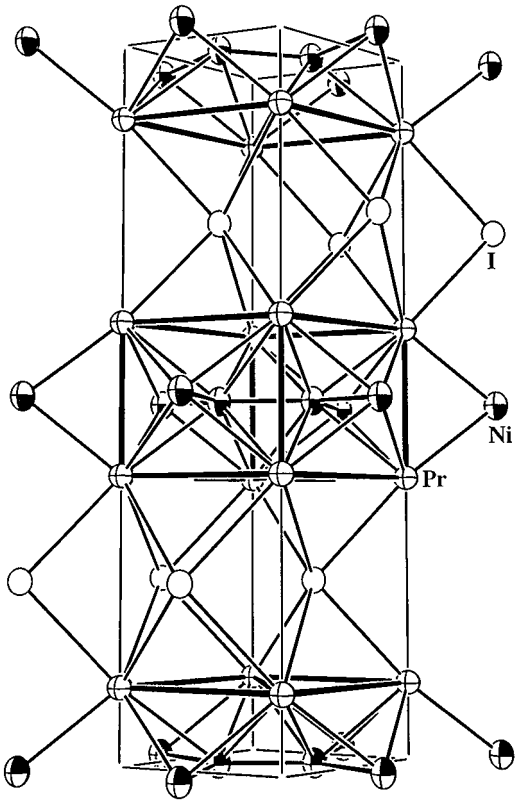

FIG. 3. Off [1$\bar{1}$0] view of one cell of Pr_2INi_2 with Pr atoms crossed, Ni shaded, and I open ellipsoids.

double-halogen-layered R_2X_2Z, $X = Cl$, Br, $Z = C$, N, etc., in which the close-packed layers are sequenced (X–R–Z–R–X) with Z in all antiprismatic sites between R–R layers (3). Analogs that are further reduced occur as Gd_2XC (X = Cl, Br, I) (12, 13) and La_2IZ, Z = Ru, Rh, Ir, Pt (14) in which only single halogen layers intervene, but still with a close-packed ordering of the layers. Naturally, the doubled number of interstitial atoms within the trigonal prismatic array of R in Gd_2IFe_2, Pr_2INi_2, La_2IFe_2, etc. bring the Z into much closer proximity. In Pr_2INi_2, the three Ni–Ni distances each correspond to a Pauling bond order (27) of 0.82, while the six Ni–Pr separations average 0.49 each if the individual single bond metallic radii are considered additive. In some contrast, the bond order for the short cross-slab Pr–Pr separation (3.665 Å, the edge of the trigonal prisms) is 0.24, while the long Pr–Pr separations within the layers corresponds to only a small bond order (0.05 each) although there are 12 times as many of these. The dimensions within the large number of cluster-based compounds of rare-earth metals that are centered by transition metals strongly suggest that the heterometal interactions must be strong.

The nature of the bonding interactions in these unusual trigonal prismatic R–Z_2–R slabs was further defined through 3D charge-consistent extended Hückel band calculations on La_2IFe_2. The total densities-of-states are shown in Fig. 5 with the La contributions projected out. The remainder of the contributions come nearly entirely from iron between -8.0 and -10.5 eV and principally from iodine therebelow. Mixing of Pr and Fe, mainly through their respective d orbitals, is appreciable in the conduction bands above -10.5 eV, but the DOS are localized primarily on Fe close to E_F (-8.3 eV). Figure 6 provides further

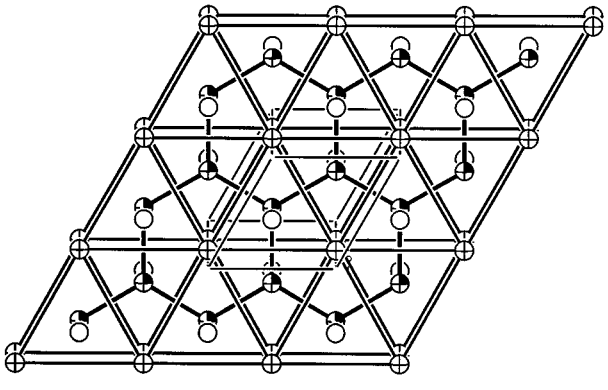

FIG. 4. ~ [001] view of one I–Pr–Ni_2–Pr–I section of Pr_2INi_2. The legend is the same as in Fig. 3.

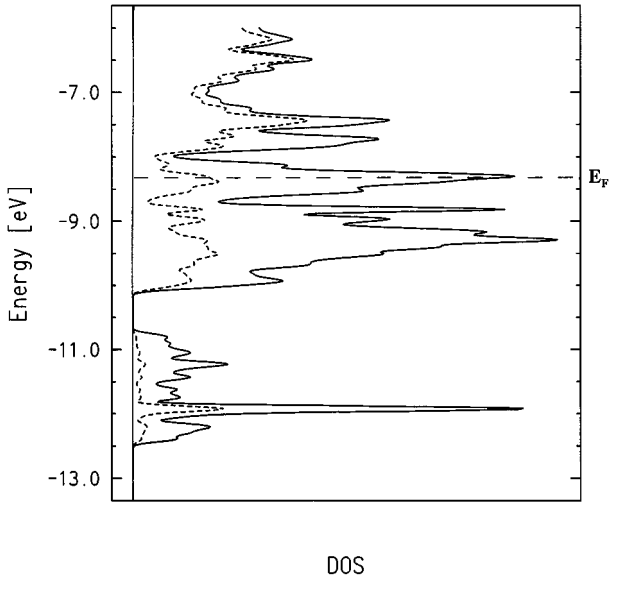

FIG. 5. Densities-of-states vs energy for La_2IFe_2 according to a charge-consistent extended-Hückel band calculation. The lanthanum contributions are shown with the dashed curve. Iron makes most of the remaining contributions in the upper band, and iodine 5p in the lower.

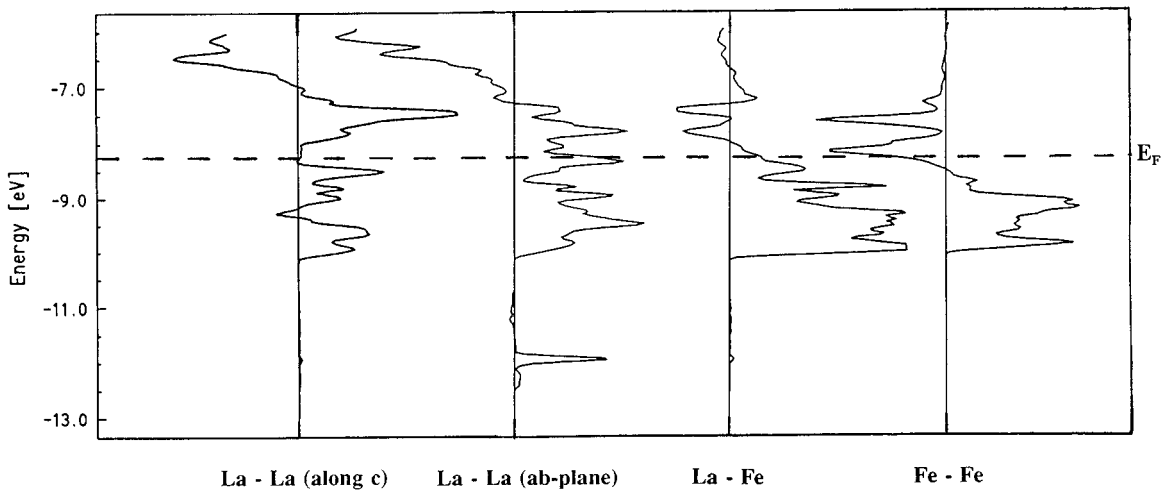

FIG. 6. COOP curves vs energy for various interactions: La–La along *c*, La–La parallel to the *a*–*b* plane, La–Fe and Fe–Fe. Overlaps out to 4.1 Å are included.

clarification through the COOP curves (overlap-weighted bond populations) as a function of energy for La–La (both parallel and normal to **c**), La–Fe, and Fe–Fe. Bonding (positive overlap) lies to the right in each. The abscissa scales for these are not directly comparable because of the overlap integral inclusions. The strong mixing of La 5*d* and Fe 3*d* states as well as Fe–Fe bonding within the slabs is particularly evident although the last is becoming unfavorable near E_F. Sizable La–La bonding is also evident. Of course, one does not gain any insight from this treatment as to why this structure forms instead of something else. Metallic conductivity behavior is clearly expected, and a range of Z seems likely in a rigid band sense. Of course, this ascertion completely ignores variations in the stability of alternate compounds, a risky condition.

These conclusions are in considerable contrast to those of Ruck and Simon regarding both $Y_2Br_2Fe_{2+x}$, an intercalated version of the same type of R_2Z_2 slabs separated by double bromine layers, and Gd_2IFe_2 (15). They found that substantially all yttrium orbital contributions lay above E_F, leading to the conclusion that the bonding in both compounds was largely heteropolar, the rare-earth metals serving mainly to donate electrons to the iron and halogen states. This unconventional and unexpected result for interactions between two transition metals in fact apparently arose because unsuitable choices for the valence energy (H_{ii}) values for the metals, which were evidently the program default values derived from very different compounds in positive oxidation states. Their Fe 3*d* energy thus fell only 0.5 eV above that for Br 4*p*, but an improbable 6.3 eV below Y 4*d*. (We similarly obtained an unreasonably large, -3 charge on Fe in $Zr_6Cl_{14}Fe$ using the default energies, even within the Mulliken approximation that divides bond populations equally between the atoms (34).) Iterative calculations in such uncommon bonding situations are necessary so that the valence energies better reflect the actual charge (oxidation) states present, which vary inversely to one another. In the present example, the iteration reduced the difference between valence *d* levels of the two metals from 4.4 to 0.9 eV. Furthermore, the H_{ii} values obtained by charge iteration for iron in La_2IFe_2 lie 0.4 to 0.9 eV above those for the element, a reasonable result. These energy dispositions must be similar to those in intermetallic compounds themselves, except for loss of some valence electrons to the electronegative halides in the present examples.

ACKNOWLEDGMENTS

Martin Köckerling assisted with the plotting of the theoretical results. This work was supported by the National Science Foundation, Solid State Chemistry, via Grants DMR-9207361 and -9510278, and was carried out in the facilities of the Ames Laboratory, U.S. Department of Energy.

REFERENCES

1. J. D. Corbett, *J. Alloys Comp.* **229,** 10 (1995).
2. J. D. Corbett, *in* "Modern Perspectives in Inorganic Crystal Chemistry" (E. Parthé, Ed.), p. 27. Kluwer Academic, Dordrecht, 1992.
3. A. Simon, Hj. Mattausch, G. J. Miller, W. Bauhofer, and R. K. Kremer *in* "Handbook on the Physics and Chemistry of Rare Earth" (K. A. Gschneidner and L. Eyring, Eds.), Vol. 15, p. 191. Elsevier Science, Amsterdam, 1991.
4. R. Llusar and J. D. Corbett, *Inorg. Chem.* **33,** 849 (1994).
5. S. J. Steinwand and J. D. Corbett, *Inorg. Chem.* **35,** 7056 (1996).
6. Y. Park and J. D. Corbett, *Inorg. Chem.* **33,** 1705 (1994).
7. M. W. Payne, P. K. Dorhout, and J. D. Corbett, *Inorg. Chem.* **30,** 1467 (1991).

8. M. W. Payne, P. K. Dorhout, S.-J. Kim, T. R. Hughbanks, and J. D. Corbett, *Inorg. Chem.* **31,** 1389 (1992).
9. P. K. Dorhout, M. W. Payne, and J. D. Corbett, *Inorg. Chem.* **30,** 4960 (1991).
10. U. Schwanitz-Schüller and A. Simon, *Z. Naturforsch. B* **40,** 710 (1985).
11. S.-J. Hwu, R. P. Ziebarth, S. v. Winbush, J. E. Ford, and J. D. Corbett, *Inorg. Chem.* **25,** 283 (1986).
12. Hj. Mattausch, C. Schwarz, and A. Simon, *Z. Kristallogr.* **178,** 156 (1987).
13. C. Bauhofer, Hj. Mattausch, G. J. Miller, W. Bauhofer, R. K. Kremer, and A. Simon, *J. Less-Common Met.* **167,** 65 (1990).
14. J. D. Martin and J. D. Corbett, unpublished.
15. M. Ruck and A. Simon, *Z. Anorg. Allg. Chem.* **619,** 327 (1993).
16. M. W. Payne and J. D. Corbett, *Inorg. Chem.* **29,** 2246 (1990).
17. P. Villars, L. D. Calvert, "Pearson's Handbook of Crystallographic Data for Intermetallic Phases," 2nd ed., Vol. 4. American Society of Metals, Metals Park, OH, 1991.
18. G. M. Sheldrick, "SHELXS-86." Universität Göttingen, Germany, 1986.
19. (a) "TEXSAN-TEXRAY, Structure Analysis Package." Molecular Structure Corp., Woodlands, TX, 1985; (b) C. J. Gilmore, *J. Appl. Crystallogr.* **17,** 42 (1984). (c) P. T. Beurskens, "DIRDIF: Direct Methods for Difference Structures." Technical Report 1984/1; Crystallography Laboratory, Toernooiveld, 6525-Ed Nijmegen, The Netherlands, 1984.
20. N. Walker and D. Stuart, *Acta Crystallogr. A* **39,** 158 (1983).
21. M. H. Whangbo, R. Hoffmann, and R. B. Woodward, *Proc. Roy. Soc. London, A* **366,** 23 (1979).
22. S. Alvarez, "Table of Parameters for Extended Hückel Calculations." Barcelona, Spain, 1987.
23. C. E. Meyers, L. J. Norman, and L. L. Loew, *Inorg. Chem.* **17,** 1581 (1978).
24. T. Hughbanks and J. D. Corbett, *Inorg. Chem.* **28,** 631 (1989).
25. S. M. Kauzlarich, T. Hughbanks, J. D. Corbett, P. Kalvins, and R. N. Shelton, *Inorg. Chem.* **27,** 1791 (1988).
26. D. Nagaki, S. Simon, and H. Borrmann, *J. Less-Common Met.* **156,** 193 (1989).
27. L. Pauling, "The Nature of the Chemical Bond," p. 400. Cornell Univ. Press, Ithaca, NY, 1960.
28. S. Sevov and J. D. Corbett, *J. Am. Chem. Soc.* **115,** 9089 (1993).
29. A. Guloy and J. D. Corbett, *Inorg. Chem.* **35,** 4669 (1996).
30. O. K. Andersen, O. Jepsen, and D. Glötzel, *in* "Highlights of Condensed-Matter Theory" (F. Bassani, F. Fumi, and F. M. P. Tosi, Eds.), p. 59, North-Holland, Amsterdam, 1985.
31. M. Ebihara, J. D. Martin, and J. D. Corbett, *Inorg. Chem.* **33,** 2079 (1994).
32. E. Warkentin and A. Simon, *Rev. Chim. Minér.* **20,** 488 (1983).
33. M. Ruck, Ph.D. Dissertation, University of Stuttgart, 1991.
34. T. Hughbanks, G. Rosenthal, and J. D. Corbett, *J. Am. Chem. Soc.* **110,** 1511 (1988).